Nanoscale

ROYAL SOCIETY OF CHEMISTRY

PAPER

View Article Online
View Journal | View Issue

Check for updates

Cite this: *Nanoscale*, 2022, **14**, 8825

Direct synthesis of Au–Ag nanoframes by galvanic replacement *via* a continuous concaving process†

Fang Cheng, [a] Wenjie Gu,[a] Han Zhang,[a] Chunyuan Song, [a] Yunfeng Zhu,[a] Feiyue Ge,[b] Kuiming Qu,[a] Hai Xu,[c,d] Xue-Jun Wu *[b] and Lianhui Wang *[a]

Received 23rd March 2022,
Accepted 13th May 2022

DOI: 10.1039/d2nr01600a

rsc.li/nanoscale

Controlled synthesis of noble-metal nanoframes is of great interest due to their promising applications in plasmonics and catalysis. However, the synthesis is largely limited to a multiple-step approach involving selective deposition followed by selective etching. Here we report a facile and general strategy to synthesize Au–Ag nanoframes based on a direct galvanic replacement reaction between Ag nanoparticles and a gold(I) complex, sodium aurothiosulfate, without an extra etching process. The formation of Au–Ag nanoframes in our approach undergoes a continuous concaving and hollowing-out process from Ag templates, which is related to selective Au deposition and the Kirkendall effect. As a proof-of-concept, it was shown that Au–Ag nanoframes with different dimensions can be prepared from the corresponding Ag nanocolloids using our strategy. The prepared wire-like Au–Ag nanoframes show superior single-particle surface-enhanced Raman scattering due to the linear narrow nanogaps within the nanoframes. We believe this study signifies a new approach by mediating galvanic replacement to prepare noble-metal nanoframes with precise controllability, which may enable a variety of applications in plasmonics and catalysis.

Introduction

Synthesis of noble-metal nanostructures with well-defined morphology and crystal structures is crucial to modulate their plasmonic and catalytic properties. Noble-metal nanoframes, hollow nanostructures with wide openings in each facet, have attracted tremendous attention in recent years due to their tunable composition and large surface area per volume, which facilitates their promising applications in catalysis,[1,2] plasmonics,[3,4] and biomedicine.[5,6] For instance, the interior nanogaps of noble-metal nanoframes, affording inherent hotspots, are found to be responsible for the enhanced performance in surface-enhanced Raman scattering (SERS).[7–9] Over the past two decades, a variety of noble-metal nanoframes with tunable composition and morphologies have been prepared *via* different synthetic routes.[10–12] One commonly used strategy is the presynthesized template-assisted method, in which faceted nanoparticles are first prepared and used as templates, followed by the selective deposition of the target metal on the vertices and edges of the templates. Finally, the nanoframes can be obtained by selective dissolution of the templates. Noble-metal nanocolloids, such as Au, Ag and Pt, with controllable shapes have been widely applied as templates to produce nanoframes.[10] Obviously, selective deposition is the key step, thus kinetic and thermodynamic control should be carefully considered in the preparation. Generally, selective deposition requires differences in surface energy for different sites of the templates. However, the deposition process is sometimes inevitably accompanied by galvanic replacement, which makes the reaction much more difficult to control.

The galvanic replacement reaction, an electrochemical process involving the oxidation of a metal by another metal ion possessing higher reduction potential,[13] provides a powerful strategy to prepare hollow nanostructures from the presynthesized template.[14–17] The prototypical case is the preparation of Au–Ag hollow nanostructures templated by Ag nanoparticles.[18–20] When a suspension of Ag nanocubes (Ag NCs) is mixed with $HAuCl_4$ solution, the galvanic replacement reaction takes place, that is, Ag NCs undergo oxidation accompanied by the reduction of Au from the ion solution. In

[a]*State Key Laboratory for Organic Electronics and Information Displays & Jiangsu Key Laboratory for Biosensors, Institute of Advanced Materials (IAM), Jiangsu National Synergetic Innovation Center for Advanced Materials (SICAM), Nanjing University of Posts and Telecommunications, Nanjing 210023, P. R. China. E-mail: iamlhwang@njupt.edu.cn*

[b]*State Key Laboratory of Coordination Chemistry, School of Chemistry and Chemical Engineering, Nanjing University, Nanjing 210023, P. R. China. E-mail: xjwu@nju.edu.cn*

[c]*Changchun Institute of Optics Fine Mechanics and Physics Chinese Academy of Science, Changchun 130033, P. R. China*

[d]*Center of Materials Science and Optoelectronics Engineering, University of Chinese Academy of Sciences, Beijing 100040, P. R. China*

†Electronic supplementary information (ESI) available. See DOI: https://doi.org/10.1039/d2nr01600a

this process, the reduced Au tends to alloy with the underlying Ag, since the homogeneous alloy is thermodynamically more stable than the mixture of segregated Au and Ag.[21] The galvanic replacement reaction leads to structural transformation from solid Ag NCs to Au–Ag nanoboxes with a hollow interior and alloyed shell. The nucleation, growth and coalescence of voids inside Ag NCs play a critical role for the hollowing-out process.[22,23] However, to produce nanoframes with wide openings in each facet by the galvanic replacement reaction, an extra etching process is usually required. Although the gold precursor itself can be used as the etchant, the unwanted coupling between the Ag dealloying and the accompanying Au deposition makes it difficult to control the shell thickness and porosity of the nanoframes. Other etchants, such as $Fe(NO_3)_3$ or NH_4OH, have also been studied, but it is still not easy to control the morphology of the products.[24] Therefore, the additional etching step not only increases the complexity of the synthesis, but also adds to the uncertainty of the structural control. To date, the successful synthesis of noble metal nanoframes by simple galvanic replacement without an additional etching process is still lacking.

Here, we report the direct synthesis of Au–Ag nanoframes *via* the galvanic replacement reaction using a gold(I) complex, sodium aurothiosulfate ($Na_3Au(S_2O_3)_2$), as the gold precursor. Interestingly, the structural evolution of the reaction reveals a continuous concaving process as well as a void formed in the center of the Ag templates due to the Kirkendall effect. The jointing of concave facets and the voids eventually leads to the formation of nanoframes with wide openings on each facet. It is noted that the final morphology of the product is highly dependent on the capping agent; Au–Ag nanoboxes with inhomogeneous alloyed walls can be obtained when PVP is used as the capping agent. Interestingly, our synthetic method can be successfully extended to the preparation of other nanoframes, such as one-dimensional (1D) and two-dimensional (2D) nanoframes, which are templated by triangular Ag nanoplates and Ag nanowires, respectively. The wire-like Au–Ag nanoframes exhibit enhanced single-particle SERS activity compared with the Au–Ag nanotubes, due to the interior narrow nanogaps within the structures. The research provides an effective and facile strategy for the controlled synthesis of noble-metal nanoframes, which is applicable to SERS and optoelectronics.

Experimental

Chemicals and materials

Ethylene glycol (EG, 99.8%, Sigma), silver trifluoroacetate (CF_3COOAg, ≥99.99%, Sigma), sodium hydrosulfide hydrate ($NaHS{\cdot}xH_2O$, Sigma), poly(vinylpyrrolidone) (PVP, $M_w \approx 55\,000$, 29 000, and 360 000, Sigma), hydrochloric acid (HCl, 37%, Sinopharm), gold(I) sodium thiosulfate hydrate ($Na_3Au(S_2O_3)_2{\cdot}2H_2O$, 99.9%, Alfa Aesar), triethanolamine (TEOA, 97%, Sigma), sodium hydrosulfide hydrate ($Na_2S_2O_3{\cdot}5H_2O$, ≥99.5%, Sigma), hexadecyltrimethylammonium bromide (CTAB, ≥99%, Sigma), hexadecyltrimethylammonium chloride (CTAC, 99%, J&K Scientific), dodecyltrimethylammonium bromide (DTAB, 99%, Mackin), *N*,*N*-dimethylformamide (DMF, 99.5%, Rhawn), silver nitrate ($AgNO_3$, 99%, Sigma), copper(II) chloride ($CuCl_2$, 99.99%, Aladdin) and Rhodamine 6G (R6G, 95%, Aladdin). All chemicals were used as received without further purification, and deionized (DI) water (18.2 MΩ cm^{-1}) was used for solution preparations.

Synthesis of Ag NCs

Ag NCs were prepared according to the published protocol.[25] After washing with acetone and DI water, the products were re-dispersed in DI water for further use.

Synthesis of Au–Ag nanoframes

5 mL of CTAB (200 mM), 1 mL of TEOA (500 mM), and 1.7 mL of DI water were mixed in a 20 mL glass vial, followed by the addition of 0.3 mL of Ag NC suspension (891 μg mL^{-1}) under magnetic stirring at 30 °C for 10 min. Then, 1 mL of $Na_2S_2O_3$ (50 mM) was added to the above mixture and stirred for another 10 min. Sequentially, 1 mL of $Na_3Au(S_2O_3)_2$ (2.4 mM) was injected into the reaction mixture, which was allowed to react at 30 °C for around 70 min. After the reaction, the products were collected by centrifugation at 11 000 rpm for 5 min and then washed with DI water for three times. To monitor the transformation process of the galvanic replacement reaction, the concentration of $Na_3Au(S_2O_3)_2$ was decreased to 40% of the original concentration (0.96 mM), while all the other parameters were kept the same. For the control experiments investigating the influence of temperature, the reaction temperature was changed from 30 °C to 40 °C and 60 °C while keeping all the other parameters the same. For the control experiments investigating the role of the capping agent, CTAB (200 mM) was replaced by CTAC (200 mM) or DTAB (200 mM), while all the other reaction conditions were kept the same.

Synthesis of Au–Ag nanoboxes

10 mg of PVP ($M_w \approx 55\,000$), 1 mL of TEOA (500 mM), and 7.7 mL of DI water were mixed in a 20 mL glass vial, followed by the addition of 0.3 mL of Ag NC suspension (891 μg mL^{-1}). Then, 1 mL of $Na_3Au(S_2O_3)_2$ (2.4 mM) was add to the above solution and reacted at 30 °C for 2 h. The synthesis was also performed with the addition of $Na_2S_2O_3$ (1 mL, 50 mM), while all the other experimental conditions were kept the same. The products were collected by centrifugation, washed with DI water twice, and then re-dispersed in DI water.

Synthesis of triangular Ag nanoplates

Triangular Ag nanoplates were synthesized according to the previous report with slight modification.[26] 138.75 mg of PVP ($M_w \approx 29\,000$) was dissolved in 25 mL of DMF, and then 4.25 mg of $AgNO_3$ was added to the above solution. After dissolving completely, the mixture was transferred to a 100 mL autoclave and heated at 150 °C for 12 h. The products were collected by centrifugation, washed twice with ethanol, and then re-dispersed in DI water for use.

Synthesis of triangular Au–Ag nanoframes

5 mL of CTAB (200 mM), 1 mL of TEOA (500 mM), and 1.126 mL of DI water was added into a 20 mL glass vial, followed by the introduction of 0.874 mL of aqueous suspension of Ag triangular nanoplates (305.64 μg mL^{-1}). The mixture was sonicated at room temperature for 4 min. Then, 1 mL of $Na_2S_2O_3$ (50 mM) was add into the glass vial under magnetic stirring at 30 °C for 30 s, followed by the addition of $Na_3Au(S_2O_3)_2$ (2.4 mM, 1 mL). After the reaction for 1 h, the products were collected by centrifugation, washed with DI water twice and re-dispersed in DI water.

Synthesis of Ag nanowires

Ag nanowires were synthesized according to the previous report with slight modifications.[27] 50 mL of EG was introduced into a 100 mL round bottom flask, followed by the addition of 500 μL of $CuCl_2$ (4 mM in EG). The mixture was heated in an oil bath set at 165 °C. Then, 15 mL of PVP solution ($M_w \approx$ 360 000, 0.15 M in EG, calculated in terms of repeating units) and 15 mL of $AgNO_3$ solution (86 mM in EG) were introduced in sequence using two injection pumps with the same rate of 3 mL min^{-1}. The reaction was allowed to continue for around 30 min. When the solution became opaque gray with wispiness, the magnetic stirring was stopped and then the solution was left for 5–10 min before quenching the reaction. The products were collected by centrifugation, washed with ethanol several times and re-dispersed in ethanol for further use.

Synthesis of wire-like Au–Ag nanoframes

5 mL of CTAB (200 mM), 1 mL of TEOA (500 mM) and 1.9062 mL of DI water were added to a 20 mL glass vial, followed by the addition of 93.8 μL of Ag nanowire suspension (2.85 mg mL^{-1}). The mixture was sonicated at room temperature for 1 min. Next, 1 mL of $Na_2S_2O_3$ (50 mM) was added to the above mixture, followed by the addition of 1 mL of $Na_3Au(S_2O_3)_2$ (2.4 mM). After reacting for about 40 min, the samples were collected by centrifugation, washed with DI water twice, and re-dispersed in 2.5 mL of ethanol for use.

Synthesis of Au–Ag nanotubes

10 mg PVP ($M_w \approx$ 55 000), 1 mL of TEOA (500 mM) and 7.9062 mL of DI water and were introduced into a 20 mL glass vial, followed by the addition of 93.8 μL of Ag nanowire suspension (2.85 mg mL^{-1}). Then 1 mL of $Na_3Au(S_2O_3)_2$ (12 mM) was added to the reaction mixture. After reacting for about 60 min, the final products were collected by centrifugation, washed with DI water twice, and re-dispersed in 2.5 mL of ethanol for use.

In situ measurement of UV–vis–NIR extinction spectra

The *in situ* UV–vis–NIR extinction spectra measurement was conducted in the Ag NCs reaction system with a 40% $Na_3Au(S_2O_3)_2$ concentration (0.96 mM). The original 10 mL reaction system was reduced to 2.5 mL and placed in a quartz cell. The Shimadu UV-2600 was used to perform the *in situ* measurement of UV–vis–NIR extinction spectra during the reaction. The spectra were recorded every 2 min within the first 10 min, and then every 10 min in the range 10–180 min.

Single-particle SERS measurements

The single-particle SERS measurements were conducted using a confocal Raman spectroscopy equipped with a 532 nm laser. A 50× objective was used to focus the laser onto the sample plane. The SERS spectra were collected using a 532 nm laser with a laser power of 0.5% of the maximum power (50 mW) and an exposure time of 10 s. The SERS mappings were obtained using the same conditions except that the exposure time was reduced to 1 s for each data point. Before SERS measurements, the samples were prepared by mixing 300 μL of the as-prepared Au–Ag wire-like nanoframes or Au–Ag nanotubes (in ethanol) with 100 μL of R6G (0.04 mM in ethanol), followed by shaking of the mixture for 30 min at 25 °C. Then, 5 μL of the mixture was dropped on a clean Si wafer and the extra mixture was sucked away after waiting for 5 s. The samples were dried under ambient conditions before single-particle SERS measurements.

Instrumentation and characterization

The transmission electron microscopy (TEM) images were taken using a Hitachi HT7700 microscope operated at 100 kV. The high-angle annular dark-field scanning TEM (HAADF-STEM) images and corresponding energy-dispersive X-ray spectroscopy (EDS) elemental mappings were acquired with a FEI Talos F200X microscope operated at 200 kV. The scanning electron microscopy (SEM) images were taken using a Hitachi S-4800 microscope. The UV–vis–NIR extinction spectra were recorded using a spectrophotometer (Shimadzu UV-3600 and UV-2600). The inductively coupled plasma mass spectra (ICP-MS) were recorded using a Nexion 2000. The SERS spectra and mappings were obtained using a Renishaw InVia confocal Raman spectrometer.

Results and discussion

In our synthesis, Ag NCs with an edge length of 45.5 ± 3.0 nm were used as the template (Fig. S1a and b†). The galvanic replacement was performed in an aqueous solution containing CTAB, $Na_2S_2O_3$ and $Na_3Au(S_2O_3)_2$, which were used as the capping agent, complexing agent, and gold precursor, respectively. Fig. 1a and b shows typical SEM and TEM images of the as-prepared Au–Ag nanoframes, which exhibit wide openings in each side facet. The nanoframes show a quite monodisperse distribution with an edge length of 47.8 ± 4.5 nm (Fig. S1c and d†), which is slightly increased compared with that of the original Ag NCs. Commonly, the cubic nanoframe can be considered as a three-dimensional structure assembled from 12 identical nanorods. In our prepared Au–Ag nanoframes, the diameters of the edges are not uniform, that is, the vertices strike larger than the middles of the edges. Sometimes, nanoframes with one or two breaking edges can be observed, which

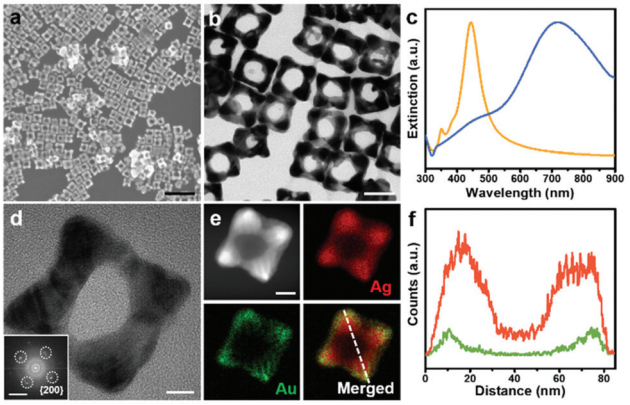

Fig. 1 Characterization of the prepared Au–Ag nanoframes. (a) SEM and (b) TEM image of Au–Ag nanoframes. (c) UV–vis–NIR extinction spectra of Ag NCs (orange line) and Au–Ag nanoframes (blue line). (d) High-resolution TEM image and the corresponding FFT pattern (inset) of a single Au–Ag nanoframe. (e) HAADF-STEM image and the corresponding EDS elemental mappings. (f) EDS line-scans recorded along the white dashed line in (e) (Ag, red; Au, green). Scale bars are 200 nm (a), 50 nm (b), 10 nm (d), 5 nm^{-1} (inset of d), and 20 nm (e).

may result from collapse due to their ultrathin structures. As shown in Fig. 1c, the prepared Au–Ag nanoframes display a broad localized surface plasmon resonance (LSPR) band peaking at 717 nm, which obviously red shifts compared with that of the Ag NCs located at 445 nm. The high-resolution TEM image of a representative Au–Ag nanoframe exhibits its high crystalline structure (Fig. 1d and Fig. S2†), and the corresponding fast-Fourier transform (FFT) pattern confirms its near single crystal structure (inset of Fig. 1d). The most adjacent four little-diffused diffraction points (marked by the white dashed circles) possess square symmetry, and the calculated interplanar distance is 0.20 nm, which can be ascribed to {200} planes considering the similarity of the lattice constant between gold and silver. The HAADF-STEM image and corresponding EDS elemental mappings of a single nanoframe clearly show that the distributions of Au and Ag are not completely overlapped, whereas Au preferentially distributes at the outer layer of the nanoframes (Fig. 1e). The corresponding line scans across the nanoframes further confirm the observation (Fig. 1f).

In order to investigate the transformation process from Ag NCs to Au–Ag nanoframes, the *in situ* UV–vis–NIR extinction spectra were measured throughout the reaction (Fig. S3†). A lesser amount of the gold precursors (40%) was added to reduce the reaction rate in order to better investigate the reaction process, especially at the early stage (see the Experimental section). After the initiation of the reaction, the LSPR intensity of Ag NCs (416 nm) gradually decreases. Concurrently, a new LSPR peak at a longer wavelength appears and gradually red shifts as the reaction proceeds. During the whole process, the full width at half maximum of the new peak apparently broadens with time. The spectra evolution in our synthesis is quite different from that of the galvanic replacement reaction between Ag NCs and $HAuCl_4$,[28,29] in which the LSPR peak of Ag NCs disappears at a very early stage, although a new LSPR peak is also formed and continuously red shifts with increasing $HAuCl_4$ volume. Obviously, the newly formed LSPR peak in our case can be attributed to the deposited Au on the Ag NCs, which is accompanied by the oxidation of the Ag templates, leading to a decrease in the LSPR intensity of Ag. However, the fact that the LSPR band of Ag is always detected during the whole galvanic replacement process indicates Ag (or Ag-rich alloy) exists throughout the reaction, even for the final products, which is consistent with the aforementioned elemental mappings of the nanoframes.

To further track the structural evolution, the intermediate products at different reaction stages were analyzed. Fig. 2a–e and f–j show TEM images and EDS elemental mappings of the products at different stages, respectively. In the beginning (reaction time t = 50 min), the gold is observed to mainly deposit at the vertices of the Ag NCs, accompanied by the appearance of the slightly concave facets of the templates (Fig. 2b and g). As the reaction progresses (t = 100 min), the concavity of the {100} facets becomes much more obvious, and most of the gold is observed to deposit on the vertices and edges (Fig. 2c and h). With the extension of reaction time (t = 120 min), the amount of Au on the vertices and edges is further increased, and the skeleton of the nanoframe starts to appear (Fig. 2d and i). Meanwhile, a void in the center of the nanostructure can be detected, indicating that the original Ag NCs have been changed from solid to hollow nanostructures. It should be noted that the formation of the void in the center of the Ag NCs results from the Kirkendall effect,[30] that is, the faster outward diffusion rate of Ag than inward diffusion rate of Au generates a net vacancy flux to form the void.[31–33] In the final stage (t = 180 min), the nanoframes with wide openings are formed due to the continuous concaving process followed

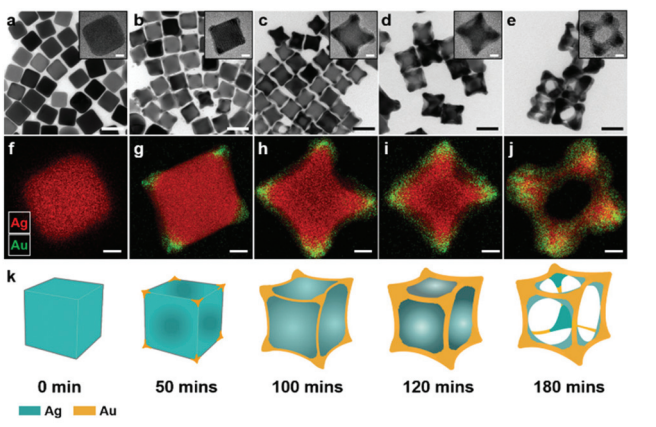

Fig. 2 Morphological evolution from Ag NCs to Au–Ag nanoframes. (a–e) Low-magnification and high-magnification (insets) TEM images of the products at different reaction stages. (f–j) EDS elemental mappings of the single nanostructure shown in the insets of (a–e). (k) Schematic illustration of the structural evolution during the reaction with the marked reaction time. Scale bars are 50 nm (a–e), 10 nm (insets of a–e), and 10 nm (f–j).

by the jointing of the concave facets and the void in the center (Fig. 2e and j). The observed distributions of Au and Ag at different reaction stages is in agreement with the acquired *in situ* UV–vis–NIR extinction spectra. According to the observed evolution process, the schematic illustration of the structural transformation during the galvanic replacement reaction is given in Fig. 2k.

The aforementioned results have demonstrated the successful preparation of Au–Ag nanoframes *via* a continuous concaving process by the galvanic replacement reaction, which is completely different from the former reports on the synthesis of Au–Ag hollow nanoboxes and nanocages.[18–20] In our synthesis, a gold(I) complex salt, $Na_3Au(S_2O_3)_2$, was used as the gold precursor for the galvanic replacement. In fact, this gold complex has been applied for 'chrysotype' since the 1840s, *i.e.*, the printing of photographs in pure gold.[34] The equation involved in this galvanic replacement reaction can be summarized as follows:

Half reactions

$$\text{Anode}: \ Ag(s) + 2S_2O_3^{2-}(aq) \rightarrow [Ag(S_2O_3)_2]^{3-}(aq) + e^-(aq) \quad (1)$$

$$\text{Cathode}: \ [Au(S_2O_3)_2]^{3-}(aq) + e^-(aq) \rightarrow Au(s) + 2S_2O_3^{2-}(aq) \quad (2)$$

Combined reaction

$$Ag(s) + [Au(S_2O_3)_2]^{3-}(aq) \rightarrow [Ag(S_2O_3)_2]^{3-}(aq) + Au(s) \quad (3)$$

The standard potential, E^0, for the above balanced reaction (3) is calculated to be 0.229 V *vs.* the standard hydrogen electrode (see the ESI†), which is obviously smaller than that of the galvanic replacement reaction between Ag NCs and $HAuCl_4$ (0.77 V).[35] The low standard potential may be the reason why Au and Ag distribute inhomogeneously in our nanoframes. Moreover, there are several merits of using the gold(I) complex salt instead of the other commonly used gold precursors, such as $HAuCl_4$[29] and AuCl.[35] Firstly, the gold(I) complex salt can easily dissolve in water with good stability, avoiding the occurrence of disproportionation reactions. Secondly, the formation of precipitated AgCl, which interferes with the epitaxial growth of Au, can be completely excluded by using the gold(I) complex salt. Last but not least, the rate of our galvanic replacement reaction is moderate, thus the gold precursor can be introduced once instead of through dropwise addition using an injection pump.

In our galvanic replacement reaction, the selective deposition of Au on vertices and edges can be interpreted as a combination of thermodynamic and kinetic controlled process. The previous studies have demonstrated the selective deposition of Au on sites with high surface energy during the galvanic replacement reaction between the Ag template and the Au ion.[36,37] Due to the relatively high curvature and low coordination number, the vertices and edges usually possess higher surface energy and higher reactivity compared with the flatter facets.[38] Therefore, the newly reduced Au atoms will initially deposit on the vertices and edges of Ag NCs. The deposited Au can stay at the original sites or migrate to other sites with lower surface energy, depending on the relative rate of deposition and diffusion. In our experiments, the selective deposition of Au when the reaction was performed at 30 °C can be interpreted as the higher reactivity of vertices/edges *versus* facets and the higher rate of deposition *versus* diffusion. However, as the temperature increases, the rates of both deposition and diffusion increase, which may produce different products. Fig. S4† shows the TEM images of the products obtained from the reaction under different temperatures. The general architecture of the nanoframes is still retained, although the higher temperature leads to nanoframes with thicker ridges and smaller holes on side facets. The morphological change in nanoframes at higher reaction temperatures can be interpreted as the overwhelming rate of diffusion *versus* deposition, leading to less selectivity of Au deposition on vertices/edges over facets.

To investigate the effect of the surfactant on the process of galvanic replacement, the reaction was also conducted using different cation surfactants, CTAC and DTAB, as the capping agents. Interestingly, the whole structural transformation also exhibits a continuous concaving process, although the reaction rate is distinct for different cation surfactants (Fig. S5†). Therefore, the transformation mechanism is independent of the anions and alkyl-carbon chain length of the cation surfactants. However, the product is completely different when the nonionic polymer, PVP, replaces CTAB as the capping agent. The product is a mixture of hollow Au–Ag nanoboxes, which consist of completely hollow structures with ultrathin shells and hollow nanostructures with eccentric Ag (Fig. S6†). Without the addition of $Na_2S_2O_3$ in the PVP synthetic solution, the reaction rate increases and the final products become monodispersed hollow nanoboxes with the LSPR band peaking at 680 nm (Fig. 3a and b). The EDS elemental mappings and line-scans confirm that Au prefers to distribute at both the inner-layer and the outer-layer of the nanobox walls (Fig. 3c and d).

According to the above results, we concluded that the temperature, capping agent and $Na_2S_2O_3$ are three critical factors for the direct synthesis of nanoframes *via* galvanic replacement. According to previous studies, the thiosulfate ion ($S_2O_3^{2-}$), compared with Br^- and PVP, has much stronger complexing ability with Ag NCs.[39–41] Therefore, the surface of Ag NCs will be passivated by $S_2O_3^{2-}$ and further neutralized by the outward CTAB bilayers when the templates are introduced into the mixture of $Na_2S_2O_3$ and CTAB. After the addition of the gold precursor, the gold is preferentially deposited on the vertices and edges of Ag NCs due to their high curvature, where the capping agent is loosely packed and easily attacked by the gold precursor. The corresponding oxidation of Ag to Ag^+ on the side facets will quickly coordinate with the $S_2O_3^{2-}$ to form $[Ag(S_2O_3)_2]^{3-}$, generating a passive layer on the surface. This passive layer can leave the surface in the presence of CTAB micelles due to electrostatic attraction. Therefore, as the reaction progress, the selective Au deposition accompanying

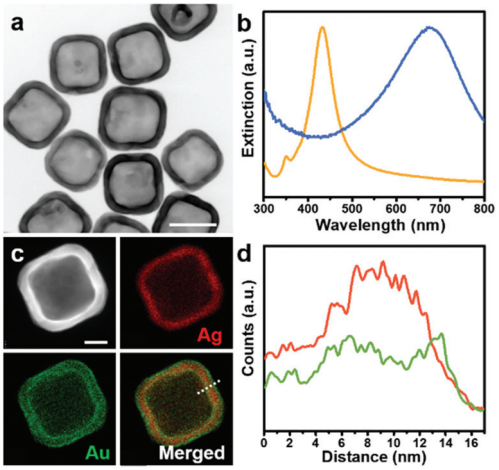

Fig. 3 Characterization of the prepared Au–Ag nanoboxes. (a) TEM image of Au–Ag nanoboxes. (b) UV–vis–NIR extinction spectra of Ag NCs (orange line) and Au–Ag nanoboxes (blue line). (c) HAADF-STEM image and EDS elemental mappings of a single nanobox. (d) EDS line-scans recorded along the white dashed line in (c) (Ag, red; Au, green). Scale bars: 50 nm (a), 20 nm (c).

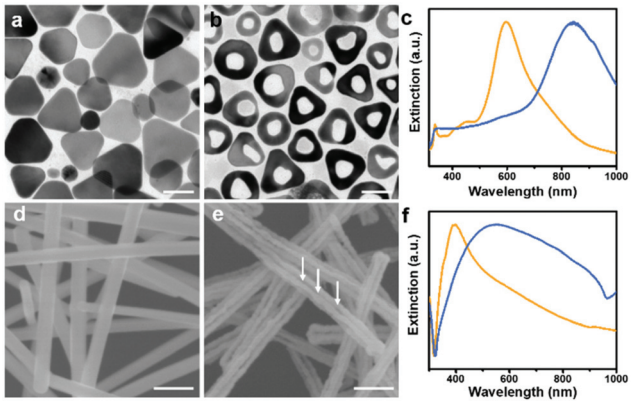

Fig. 4 The extension of the synthesis method to different Ag templates. (a and b) TEM images of triangular Ag nanoplates (a) and triangular Au–Ag nanoframes (b). (c) UV–vis–NIR extinction spectra of triangular Ag nanoplates (orange line) and triangular Au–Ag nanoframes (blue line). (d and e) SEM images of the five-fold twinned Ag nanowires (d) and wire-like Au–Ag nanoframes (e). The white arrows mark the linear-shaped nanogaps in nanoframes. (f) UV–vis–NIR extinction spectra of the Ag nanowires (orange line) and the wire-like Au–Ag nanoframes (blue line). Scale bars: 50 nm (a and b), 200 nm (d and e).

the gradual Ag oxidation results in concave facets of Ag NCs. Meanwhile, a void can form in the center of the Ag NCs due to the Kirkendall effect. Eventually, the increased concavity of the side facets, coupled with the enlarged void in the center, leads to the formation of Au–Ag nanoframes with wide openings in each side facet. When changing the capping agent to PVP, the products became nanoboxes, which is quite similar to the reported galvanic replacement between Ag NCs and $HAuCl_4$ using PVP as the capping agent.[18–20] For our galvanic replacement that took place in the PVP reaction solution, the passive layers of the formed $[Ag(S_2O_3)_2]^{3-}$ might not be easily removed from the surface due to the bulky structure and electric neutrality of the polymer PVP, which could reduce the reaction rate and lead to heterogeneity of the products. However, without the addition of $S_2O_3^{2-}$, the capping layer is missing, so that the galvanic replacement can proceed smoothly to form hollow nanoboxes. All of these discussions are in agreement with our experimental observations.

Interestingly, our method can be also extended to prepare Au–Ag nanoframes with other morphologies when the different Ag nanocolloids are used as templates. Fig. 4b shows the TEM image of the prepared 2D triangular Au–Ag nanoframes using triangular Ag nanoplates as templates (Fig. 4a). The LSPR peak red shifts from 596 nm to 840 nm after the reaction, which is in agreement with the structural transformation of the products (Fig. 4c). Moreover, the 1D wire-like Au–Ag nanoframes can also be obtained using five-fold twinned Ag nanowires as the templates (Fig. 4d and e). The as-obtained nanoframe is composed of five parallel nanowires with narrow trenches in between (white arrows in Fig. 4e), which result from the selective deposition of Au on the edges of the five-fold twinned Ag nanowires. The reaction products can be easily switched to Au–Ag nanotubes once the capping agent is changed from CTAB to PVP (Fig. S7†), which is consistent with our findings in the Ag NC reaction system. The triangular Ag nanoplates and the five-fold twinned Ag nanowires are covered by (111) and (111)/(100) facets, respectively. Although the exposed facets are different from those of the Ag NCs, the selectivity of galvanic replacement in both cases is quite obvious, where Au was deposited on the edges/vertices of the templates due to its high surface energy and Ag was oxidized from the remaining facets.

Our synthesized Au–Ag nanoframes with distinct morphologies are representative of plasmonic nanostructures with controlled interior nanogaps. The small intragaps can lead to a highly localized electronic field, which plays an important role in SERS applications.[42] As a proof-of-concept, the SERS performance of the wire-like Au–Ag nanoframe with interior narrow trenches was evaluated by measuring the single-particle SERS using R6G as the Raman reporter molecule. The nanoframes were exposed to 1.0×10^{-5} M of R6G followed by dispersal on a Si wafer, and then each nanoframe of length around 3 μm was monitored using an optical microscope while performing SERS measurements. After the measurements, the samples were checked using SEM to identify whether the SERS signal comes from a single particle or not. Fig. 5b show the SERS spectra taken from four individual spots, which are marked by dashed circles in Fig. 5a. All samples give strong SERS signals of the characteristic peaks of R6G at 1362 cm^{-1}, 1512 cm^{-1}, and 1648 cm^{-1}.[43] The SEM image further confirms the SERS signal comes from a single nanoframe (inset of Fig. 5a and Fig. S8†). The SERS mapping of a single particle exhibits a homogeneous signal distribution throughout the wire-like nanoframe (inset of Fig. 5a). In contrast, the same experiments were also conducted for the Au–Ag nanotubes to investigate their SERS performance. As shown in

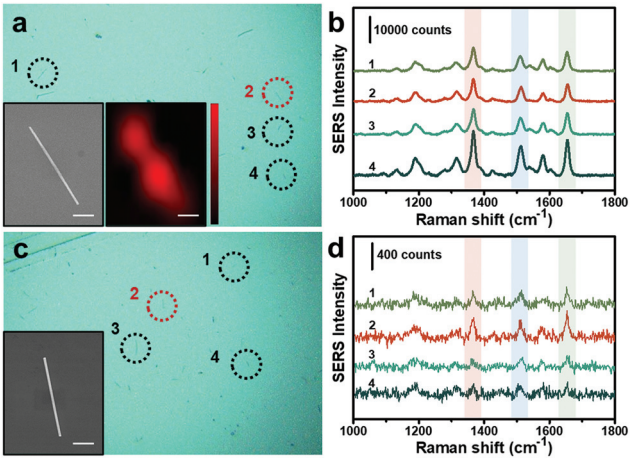

Fig. 5 Single-particle SERS measurements of the synthesized wire-like Au–Ag nanoframes and nanotubes. (a) Optical microscope image, SEM image and the corresponding SERS mapping of the Au–Ag wire-like nanoframes. The SEM image and the corresponding SERS mapping were taken from a single Au–Ag wire-like nanoframe labelled as number 2 in (a). (b) SERS spectra of R6G taken from the four different Au–Ag wire-like nanoframes marked in (a). (c) Optical microscope image and SEM image of the Au–Ag nanotubes. The SEM image was collected from the single Au–Ag nanotube labelled number 2 in (c). (d) SERS spectra of R6G obtained from the four Au–Ag nanotubes marked in (c). All the scale bars are 1 μm.

Fig. 5c and d, the SERS spectra taken from the single nanotube display significantly reduced signals. The SERS intensities at the characteristic peaks of R6G were used to compare the SERS performance of the as-prepared wire-like nanoframes and nanotubes. The average SERS intensities of the wire-like nanoframe are about 50-fold stronger than those of the nanotube. The superior SERS performance of nanoframes compared with nanotubes can be attributed to the linear-shaped narrow gaps within the nanoframes, which are absent in nanotubes.

Conclusions

In summary, we have developed a general and straightforward strategy to prepare a variety of Au–Ag nanoframes with various morphologies by a direct galvanic replacement reaction between Ag nanoparticles and gold(I) complex, sodium aurothiosulfate. Significantly, an interesting selective deposition of gold and continuous concaving process was observed during the formation of the nanoframes. It is also revealed that the choice of capping agent and temperature, and the addition of $S_2O_3^{2-}$ have a great effect on the final morphologies of the products. The hollow Au–Ag nanoboxes with inhomogeneous Au–Ag alloyed walls can be synthesized by simply switching the capping agent from CTAB to PVP. As a proof-of-concept, the 1D wire-like Au–Ag nanoframes and the 2D triangular Au–Ag nanoframes were also successfully prepared by our synthetic strategy using the corresponding Ag templates. Owing to the interior nanogaps, the SERS performance of the wire-like Au–Ag nanoframes was evaluated. It was found that the average SERS intensities of R6G from a single-particle wire-like nanoframe are about 50-fold stronger than those from the nanotube. The synthetic approach reported in this study signifies a new route to prepare noble-metal nanoframes with precise controllability, which facilities future applications in plasmonics and catalysis.

Conflicts of interest

There are no conflicts to declare.

Acknowledgements

This work was financially supported by the National Key Research and Development Program of China (2017YFA0205302), the National Natural Science Foundation of China (21902079, 21871129, 12074372), the Natural Science Foundation of Jiangsu Province of China (BK20190724), the Jiangsu Specially-Appointed Professor Plan (RK030STP19002), the Science Foundation of Nanjing University of Posts and Telecommunications (NY219136), the 1311 Talents Program of Nanjing University of Posts and Telecommunications, and the Open Project of the State Key Laboratory of Luminescence and Applications (SKLA-2020-08).

Notes and references

1 Z. Fang, Y. Wang, C. Liu, S. Chen, W. Sang, C. Wang and J. Zeng, *Small*, 2015, **11**, 2593–2605.
2 L. Xiong, Z. Sun, X. Zhang, L. Zhao, P. Huang, X. Chen, H. Jin, H. Sun, Y. Lian, Z. Deng, M. H. Rummerli, W. Yin, D. Zhang, S. Wang and Y. Peng, *Nat. Commun.*, 2019, **10**, 3782.
3 M. A. Mahmoud and M. A. El-Sayed, *J. Am. Chem. Soc.*, 2010, **132**, 12704–12710.
4 L. Zhang, T. Liu, K. Liu, L. Han, Y. Yin and C. Gao, *Nano Lett.*, 2015, **15**, 4448–4454.
5 Q. Wang, H. Wang, Y. Yang, L. Jin, Y. Liu, Y. Wang, X. Yan, J. Xu, R. Gao, P. Lei, J. Zhu, Y. Wang, S. Song and H. Zhang, *Adv. Mater.*, 2019, **31**, 1904836.
6 B. Shan, L. Li, Y. Zhao, H. Wang and M. Li, *Adv. Funct. Mater.*, 2021, **31**, 2103186.
7 W. S. Chew, S. Pedireddy, Y. H. Lee, W. W. Tjiu, Y. Liu, Z. Yang and X. Y. Ling, *Chem. Mater.*, 2015, **27**, 7827–7834.
8 J. Kim, S. Yoo, J. M. Kim, S. Choi, J. Kim, S. J. Park, D. Park, J. M. Nam and S. Park, *Nano Lett.*, 2020, **20**, 4362–4369.
9 D. Kim, J. Lee, S. Yoo, S. Choi, D. Park and S. Park, *Anal. Chem.*, 2020, **92**, 1972–1977.
10 T. Kwon, M. Jun and K. Lee, *Adv. Mater.*, 2020, **32**, 2001345.
11 T. H. Yang, J. Ahn, S. Shi, P. Wang, R. Gao and D. Qin, *Chem. Rev.*, 2020, **121**, 796–833.

12 S. Yoo, J. Kim, S. Choi, D. Park and S. Park, *Nat. Commun.*, 2019, **10**, 5789.
13 X. Xia, Y. Wang, A. Ruditskiy and Y. Xia, *Adv. Mater.*, 2013, **25**, 6313–6333.
14 J. Chen, B. Wiley, J. McLellan, Y. Xiong, Z. Y. Li and Y. Xia, *Nano Lett.*, 2005, **5**, 2058–2062.
15 J. E. Macdonald, M. Bar Sadan, L. Houben, I. Popov and U. Banin, *Nat. Mater.*, 2010, **9**, 810–815.
16 F. Xiao, B. Yoo, K. H. Lee and N. V. Myung, *J. Am. Chem. Soc.*, 2007, **129**, 10068–10069.
17 M. H. Oh, T. Yu, S.-H. Yu, B. Lim, K.-T. Ko, M.-G. Willinger, D.-H. Seo, B. H. Kim, M. G. Cho, J.-H. Park, K. Kang, Y.-E. Sung, N. Pinna and T. Hyeon, *Science*, 2013, **340**, 964–968.
18 Y. Sun and Y. Xia, *Science*, 2002, **298**, 2176–2179.
19 Y. Sun and Y. Xia, *J. Am. Chem. Soc.*, 2004, **126**, 3892–3901.
20 M. H. Kim, X. M. Lu, B. Wiley, E. P. Lee and Y. N. Xia, *J. Phys. Chem. C*, 2008, **112**, 7872–7876.
21 H. Shi, L. Zhang and W. Cai, *J. Appl. Phys.*, 2000, **87**, 1572–1574.
22 S. W. Chee, S. F. Tan, Z. Baraissov, M. Bosman and U. Mirsaidov, *Nat. Commun.*, 2017, **8**, 1224.
23 J. G. Smith, Q. Yang and P. K. Jain, *Angew. Chem., Int. Ed.*, 2014, **53**, 2867–2872.
24 X. Lu, L. Au, J. McLellan, Z. Y. Li, M. Marquez and Y. Xia, *Nano Lett.*, 2007, **7**, 1764–1769.
25 Q. Zhang, W. Li, L. P. Wen, J. Chen and Y. Xia, *Chem. – Eur. J.*, 2010, **16**, 10234–10239.
26 H. Qian, M. Xu, X. Li, M. Ji, L. Cheng, A. Shoaib, J. Liu, L. Jiang, H. Zhu and J. Zhang, *Nano Res.*, 2016, **9**, 876–885.
27 K. E. Korte, S. E. Skrabalak and Y. N. Xia, *J. Mater. Chem.*, 2008, **18**, 437–441.
28 J. Chen, B. Wiley, Z. Y. Li, D. Campbell, F. Saeki, H. Cang, L. Au, J. Lee, X. Li and Y. Xia, *Adv. Mat.*, 2005, **17**, 2255–2261.
29 S. E. Skrabalak, L. Au, X. Li and Y. Xia, *Nat. Protoc.*, 2007, **2**, 2182–2190.
30 A. D. Smigelskas and E. O. Kirkendall, *Trans. AIME*, 1947, **171**, 130–142.
31 Y. D. Yin, R. M. Rioux, C. K. Erdonmez, S. Hughes, G. A. Somorjai and A. P. Alivisatos, *Science*, 2004, **304**, 711–714.
32 W. Wang, M. Dahl and Y. Yin, *Chem. Mater.*, 2012, **25**, 1179–1189.
33 Z. Yang, N. Yang and M.-P. Pileni, *J. Phys. Chem. C*, 2015, **119**, 22249–22260.
34 M. Ware, *Gold Bull.*, 2006, **39**, 124–131.
35 L. Au, X. Lu and Y. Xia, *Adv. Mater.*, 2008, **20**, 2517–2522.
36 X. Hong, D. Wang, S. Cai, H. Rong and Y. Li, *J. Am. Chem. Soc.*, 2012, **134**, 18165–18168.
37 D. Wan, X. Xia, Y. Wang and Y. Xia, *Small*, 2013, **9**, 3111–3117.
38 Z. Nie, D. Fava, E. Kumacheva, S. Zou, G. C. Walker and M. Rubinstein, *Nat. Mater.*, 2007, **6**, 609–614.
39 S. Zhang and M. J. Nicol, *J. Appl. Electrochem.*, 2003, **33**, 767–775.
40 B. Liu, Z. Ma and K. Li, *J. Nanosci. Nanotechnol.*, 2011, **11**, 5001–5006.
41 X. Wang, L. Chen and L. Chen, *Microchim. Acta*, 2013, **181**, 105–110.
42 J. M. Kim, C. Lee, Y. Lee, J. Lee, S. J. Park, S. Park and J. M. Nam, *Adv. Mater.*, 2021, **33**, 2006966.
43 K. Wang, D. W. Sun, H. Pu and Q. Wei, *Talanta*, 2019, **195**, 506–515.